Solar Energy 173 (2018) 984–992

Contents lists available at ScienceDirect

Solar Energy

journal homepage: www.elsevier.com/locate/solener

Review

Solar energy on the Tibetan Plateau: Atmospheric influences

Nuozhen Gelsor[a,*], Norsang Gelsor[b], Tsoja Wangmo[b], Yi-Chun Chen[a], Øyvind Frette[a], Jakob J. Stamnes[a], Børge Hamre[a]

[a] Department of Physics and Technology, University of Bergen, N-5007 Bergen, Norway
[b] Lhasa Jiangsu Road No. 36, Tibet University, 850000, People's Republic of China

ARTICLE INFO

Keywords:
Solar energy
Tibet
Cloud
Aerosol

ABSTRACT

Solar energy utilization is expected to be increasingly important in order to meet future energy needs and limit CO_2 emissions to the atmosphere. To quantify the solar energy potential on the Tibetan Plateau, we have analyzed global horizontal irradiance (GHI) measurements for a three-year period at four sites with different aerosol and cloud conditions. The measurements indicate a very large solar energy potential on the Tibetan Plateau, with a small portion of GHI values even exceeding the corresponding top-of-the-atmosphere (TOA) value. Compared to a hypothetical sky condition without aerosols and clouds all year, aerosols were found to reduce the annual irradiation by about 3–6%, and the combined reduction by aerosols and clouds was found to be at most 23%. This reduction is very low compared to that at other sites around the world. For example, the west coast of Norway has a cloud/aerosol reduction effect of almost 50%, and Beijing has an estimated aerosol reduction effect of 35%. In Lhasa, Tibet the annual irradiation was found to be 7.6 GJ m^{-2}, which is 85% of the corresponding annual irradiation at the TOA.

1. Introduction

In recent years, solar energy has played a major role in the global energy transformation trend. Solar photovoltaic (PV) system has become one of the top three electricity sources in Europe. Since 2011, the global total installed solar PV capacity has increased more than three times from 69 GW to 229.3 GW by the end of 2015. In 229.3 GW, China shares 43.3 GW, which is 18.9% of total installed capacity. Germany occupies 39.6 GW (17.3%) and Japan takes 34.3 GW (15.0%). China now is leading global PV market with largest share of total installed capacity (Europe, 2016).

In a recent study of hourly solar irradiance in the period from 2001 to 2010 of about 200 sites in China, Tibet was found to have the highest annual PV capacity factor, which indicates highest annual solar power resources. The next provinces were Yunnan, Hainan, West Inner Mongolia, Gansu and Ningxia (He and Kammen, 2016).

The PV industry requires realistic statistics of solar resource during the development period (plant location) and also anticipation for possible variations of this resource during exploitation stage (energy storage). The most common parameter used to express solar resource is the global horizontal irradiance (GHI) [W m^{-2}], which is the total amount of solar energy falling on a horizontal surface per unit area per unit time integrated over the solar spectrum. The GHI is the sum of the direct normal irradiance (DNI) and the diffuse horizontal irradiance (DIF).

In spite of the importance of solar statistics, ground-based solar irradiance observation sites are not widely spread around the world. Most solar irradiance data are based on satellite-observations combined with modeling and have large spatial coverage. Such estimates need to be complemented with accurate ground measurements to improve their local accuracy, since satellite algorithms do not take into account local effects due to e.g. high mountains, desert, and snow (Suri and Cebecauer, 2014; Cebecauer and Suri, 2016; Polo et al., 2016). China has 130 observation sites for measuring the solar irradiance, but this number is only 6% of the number of widely distributed meteorological stations (Chen et al., 2014; CMA, 2017). In the US and globally, only 1% and 0.2%, respectively, of the meteorological stations have solar energy observations (Thornton and Running, 1999; Wilcox, 2012). According to information from Bureau of Meteorology (BOM, 2017) (last updated 16 Nov 2017), Australia has one-minute solar irradiance measurements at 21 stations, but only 9 of these stations are running long-term with data available at World Radiation Data Centre (WRDC) (WRDC, 2016). The main reason of this shortage of solar irradiance measurements is due to the high cost associated with operation and maintenance of ground-based instruments (Sengupta et al., 2017).

* Corresponding author.
E-mail addresses: Nuozhen.Gelsor@student.uib.no (N. Gelsor), cjwm@utibet.edu.cn (T. Wangmo), Yi-Chun.Chen@uib.no (Y.-C. Chen), Oyvind.Frette@uib.no (Ø. Frette), Jakob.Stamnes@uib.no (J.J. Stamnes), Borge.Hamre@uib.no (B. Hamre).

https://doi.org/10.1016/j.solener.2018.08.024
Received 22 May 2017; Received in revised form 13 July 2018; Accepted 10 August 2018

Without sufficiently large coverage of long-term solar irradiance measurements, it is difficult to infer local and atmospheric influences on the solar energy reaching the surface. In this paper, we investigate the locations that have high solar potential, but in a terrain which is difficult for satellite-based models.

Variation of solar energy resource is primarily caused by aerosol and cloud effects. In 2013, Calinoiu et al. in Romania showed the aerosol pollution events were estimated to cut off collectable solar energy over 20%. Further, the research group concluded that the aerosol pollution episodes should be considered in both development and exploiting stage of solar energy collection (Calinoiu et al., 2013). In our study, we have mainly analysed aerosol and cloud effect on the receivable solar energy in Tibet.

The Tibetan Plateau, located in the south west of China, is the world's largest and highest plateau (2.3×10^6 km^2, 4500 m average altitude). The world's over-all average annual solar energy potential is around 5.6 GJ m^{-2} or 1.6 MWh m^{-2} (Jaques et al., 2010). The highest solar energy potential is in the Atacama desert/plateau, Chile. However, the Sahara desert, which has the largest potential in terms of irradiation times area, can receive up to about 9.4 GJ per unit area. The Tibetan Plateau has the highest solar energy potential in China, and has the second highest solar energy potential worldwide after the Sahara desert (Wang and Qiu, 2009). There are two reasons for the rich solar resource in Tibet. First, Tibet is situated at low latitudes (27–39 °N) with high solar elevations (86–73.9°) at solar noon at the summer solstice and therefore high levels of incoming solar radiation. Second, the average altitude of the Tibetan Plateau exceeds 4500 m, which makes the atmosphere thin and highly transparent for solar radiation.

Due to the lack of fossil fuel (coal and oil) in Tibet, other sources of energy are essential to modernize the region. Solar energy is an optimal choice because of its high potential and the large land area coverage in Tibet. In the last decade, many big solar power plants (each with an electric-power production of about 10 MW) were established across the Tibetan Plateau and connected to the power grid. Almost every house in a Tibetan city has a solar water heating system on the roof top.

In this study, we present GHI data measured in one-minute intervals by pyranometers in the period 2010–2013 at four sites on the Tibetan Plateau. Also, we use an accurate radiative transfer model (AccuRT, 2017; Hamre et al., 2014) to estimate the influence of aerosol and cloud on the solar energy reaching the ground. Our study will provide important knowledge of the solar energy potential on the high-altitude Tibetan Plateau, and the measurements will serve as references for model simulations (Li et al., 2011; Tang et al., 2010; Yang et al., 2006) and contribute to the GHI data network. In addition to that, our result will contribute to both development and exploiting stage of solar energy collection in Tibetan Plateau.

The remainder of the paper is divided into three parts. In section two we describe the four sites at which the GHI measurements took place, the broad-band and spectral GHI instruments, and the modeling method (AccuRT). In section three, we discuss in detail the GHI observations and the influence of clouds and aerosols. Finally, conclusions are presented in section four.

2. Methodology

2.1. Irradiance observation sites on the Tibetan Plateau

The broad-band GHI measurements were conducted on the Tibetan side of the Himalaya range with its snow-covered mountain chain. A pyranometer was installed at each of four sites in Tibet, namely in Lhasa, Nagchu, Tingri, and Nyingchi (Fig. 1). At all four sites, the weather bureau records meteorology statistics and irregular discontinuous solar radiation measurements (personal communication). The solar radiation data are neither published nor accessible.

Lhasa (29.65 °N, 3683 m) is the capital city of the Tibet Autonomous Region. It is situated in the southeast of Tibet, and has about 3000 sunshine hours per year (WeatherChina, 2016). Its location in a valley protects Lhasa from extreme temperatures as well as strong winds. Lhasa generally has a dry and cool semi-arid climate with about 480 mm annual precipitation (Tutiempo, 2016). In Lhasa, the broad-band GHI measurements were recorded in the period from July 2010 to September 2012.

Nagchu (31.47 °N, 4510 m) is located in Northern Tibet, and receives 2850 to 2900 sunshine hours per year (WeatherChina, 2016). It is covered mostly by grass land, small hills, and a few high mountains. Northern Tibet plays an important role for the water supply and for the stock-breeding on the Tibetan Plateau. Nagchu has a sub-frigid, semi-arid, monsoon climate with long cold winters and short summers, and has an average annual precipitation of 500 mm (Tutiempo, 2016). The broad-band GHI measurements took place in the period from July 2010 to September 2013.

Tingri (28.66 °N, 4335 m) lies next to the south border of Tibet, only about 60 km from the foot of Mt. Everest. The GHI at Mt. Everest is affected by various climatic factors, such as ice and snow coverage and precipitation. Tingri is located in the semi-arid monsoon climate zone. The number of yearly sunshine hours reaches about 3400 (WeatherChina, 2016), and the average annual precipitation is about 300 mm (Tutiempo, 2016). The high number of sunshine hours indicates that Tingri is the site with the highest solar energy potential. In Tingri, broad-band GHIs were measured first for half a year starting from July 2010, and then for about seven months, starting from April 2012. This non-continuous measurement period was due to instrument maintenance difficulty.

Nyingchi (29.66 °N, 2995 m) is the lowest and easternmost site, situated about 30 km away from the Brahmaputra river. The Northern Himalaya mountains and the Nyenchen Tanglha mountains form the valley landform of Nyingchi, and protects it, like Lhasa, from extreme weather. A rather low surface albedo is observed in Nyingchi throughout the year. Due to warm winds from India, Nyingchi has a semi-humid monsoon climate. The number of sunshine hours reaches about 2000 (WeatherChina, 2016), and the average annual precipitation is 680 mm (Tutiempo, 2016). It seldom snows in Nyingchi. Broad-band GHIs were measured for half a year in Nyingchi starting from July 2010.

To obtain the annual mean temperature and precipitation for each of the four sites we have used TuTiempo.net, which has historical weather records for over 8000 weather stations worldwide.

2.2. Instrumentation

2.2.1. Irradiance instrumentation

The irradiance measurements were recorded by Pyranometer CMP6 instruments (Kipp & Zonen), which measure the GHI integrated over the broad spectral band from 310 to 2800 nm. The CMP-6 Pyranometer is based on the thermoelectric detection principle and has a blackened horizontal surface that absorbs more than 97% of the incoming radiation over its wide band of wavelengths. Measurements were recorded every minute as one-minute averages. The daily uncertainty is 5%, and the sensitivity of each thermopile is unique. Therefore, each pyranometer has its unique calibration factor. All four pyronameters were calibrated before delivery, and then calibrated again every two years in Beijing. The CMP-6 Pyranometers were calibrated against CMP-22 Pyranometers (uncertainty = 0.6%) which are traceable to international standards of measurement. It is necessary to carry out surface cleansing of the dome once per 10 days. In the summer mornings of Nyingchi and Nagchu, dew is commonly formed. At Lhasa and Tingri, dusty and windy weather can be expected during winter time. Three to four times of inspection were conducted every year with cleaning and leveling. Unrecorded and incomplete data were registered as no value and appear white in Fig. 3. Instrument specifications can be found on the Kipp & Zonen official website: http://www.kippzonen.com. A correction could be needed when comparing measurements with results

Fig. 1. Measurement sites (yellow dots) in the Himalayan mountain region. Map data: Google, Landsat.

obtained using a plane-parallel radiative transfer model, such as AccuRT, which does not account for shadowing by possible mountains surrounding an observation site. Thus, a modeled GHI could possibly be slightly larger than the measured GHI.

In this study, we follow the irradiance measurement quality control method published in 2008 (Long and Shi, 2008). In Fig. 2 we present two days of measured summer GHI in Lhasa and Nagchu (purple dots), including some very high values caused by cloud enhancement. Blue curve represents the BSRN physically possible maximum limits. Red and orange curves represent the climatological limits (1st and 2nd level configurable limits). Sun-Earch distance variation in a year induced the "thickness" of the curves. The configuration limits are derived from historical data analyses at each site. Here we use the testing limits determined in the Southern Great Plains (SGP) of the continental USA. Most data fall below the 1st level limit as expected. Very few data points are above 2nd level limit due to cloud enhancement. Here, 1st level are the smallest testing limits, 2nd level are the second limits set for data value being tested to be −9999.0 caused by failure.

2.2.2. Spectral GHI instrumentation

The spectral GHI was measured at a few sites to provide information about aerosol composition and anthropogenic gases in the atmosphere. This information is used to estimate how aerosols affect the solar energy reaching the ground. In this study, two sites in Tibet (Lhasa, 29.65 °N, 3683 m; Shegatse, 29.25 °N, 3837 m, 250 km west of Lhasa) are compared with two sites in mainland China (Beijing, 39.93 °N, 50 m; Chengdu, 30.68 °N, 500 m) in order to estimate differences in air condition.

The TriOS Ramses-ACC-VIS and Ramses-ACC-UV instruments measure the spectral GHI [W m^{-2} nm^{-1}] in the wavelength bands 320–950 nm and 280–500 nm, respectively. The detector is a 256 channel silicon photo-diode array. Each channel has a bandwidth of about 10 nm Full Width at Half Maximum. The spectral accuracy is ± 0.3 nm for RAMSES-ACC-VIS and ± 0.2 nm for RAMSES-ACC-UV. The accuracy for each instrument is better than 6–10%. More instrument specifications can be found on the TriOS official website: http://www.Trios.de.

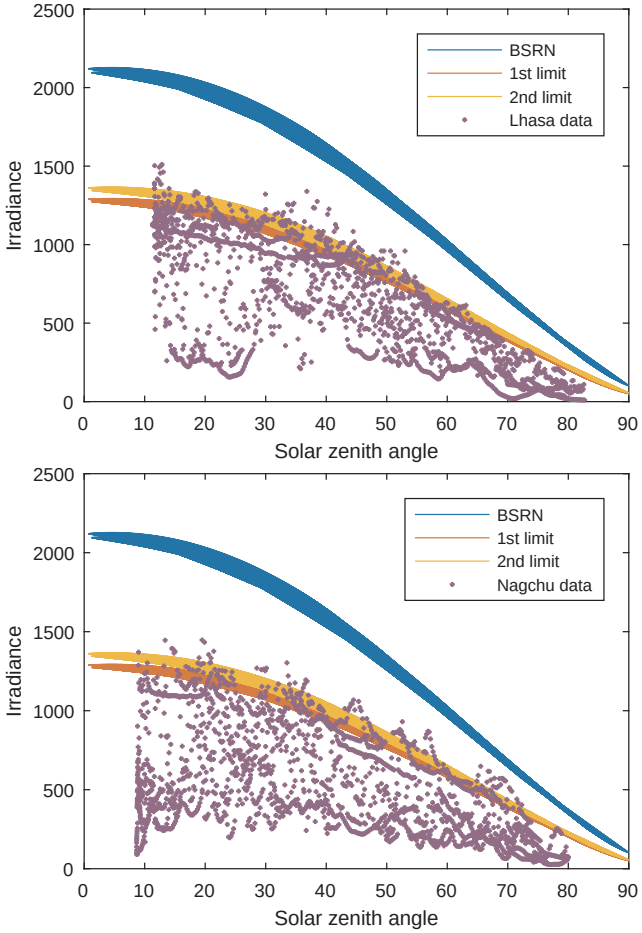

Fig. 2. 1 min variations of measured GHI during summer time at Lhasa and Nagchu site. 1st (red) and 2nd (orange) level configurable limits and BSRN (blue) physically possible maximum limits are also shown here. (For interpretation of the references to colour in this figure legend, the reader is referred to the web version of this article.)

2.3. Modeling method – AccuRT

In order to investigate how clouds and aerosol influence the broadband solar energy reaching the ground, we used an accurate radiative

transfer tool (AccuRT, 2017; Hamre et al., 2014; Stamnes et al., 2017) to simulate the spectral ground GHI under sky conditions without aerosols and clouds, as well as spectral GHIs for different aerosol and cloud optical depths and solar elevations. AccuRT uses a similar radiative transfer solver as other common radiative transfer packages that could be used for solar energy modeling, such as LibRadtran (Mayer and Kylling, 2005). Note that LibRadtran shares a similar radiative transfer solver with AccuRT and is a recognized widely used free software in the solar community. In addition, AccuRT has a coupling to a possible lower slab with a different refractive index, making it suitable as general radiative transfer tool for both the atmosphere and ocean. AccuRT solves the Radiative Transfer Equation (RTE) for any horizontal layer in a vertically stratified atmosphere-surface system with known inherent optical properties in each layer. Detailed calculation of spectral radiance in each layer is specified in (Stamnes et al., 2017).

AccuRT applied the same TOA spectrum as in libRadtran. A comparison between this spectrum and two standard extraterrestrial spectra (Wehrli, 1985; Neckel, 1981), showed only 2–3% mean difference. AccuRT solves the RTE for a coupled system consisting of two slabs, an upper atmospheric slab and a slab that may contain a material with different refractive index, such as water. In the present case, we consider a land surface, which is handled in AccuRT by letting the material in a thin lower slab be vacuum. For simplicity, the bottom of the lower slab is chosen to have an albedo of a Lambertian reflector with spectral dependence given by that of a sandy bottom surface (albedo = 0.3 at 588 nm), chosen to mimic a semi-arid Tibetan environment.

For the atmosphere-surface configuration specified above, AccuRT was used to solve RTE by: (i) dividing the atmosphere into a sufficiently large number of homogeneous horizontal layers, in each of which the optical properties remain constant; (ii) using the discrete-ordinate method to solve the RTE to obtain the spectral diffuse radiance in each horizontal layer by converting the integro-differential RTE into a system of coupled ordinary differential equations; (iii) applying continuity of the diffuse spectral radiance at each interface between different horizontal atmospheric layers; (iv) applying boundary conditions at the TOA (no incoming diffuse radiation) and at the surface (Lambertian reflector); (v) integrating the spectral diffuse radiance and the spectral radiance in the direct solar beam over the wavelength band 310–2800 nm to obtain the broad-band solar radiance for a given zenith angle; (vi) integrating the broad-band solar radiance for a given zenith angle that is incident at the surface times the cosine of the polar angle over the downward hemisphere to obtain the broad-band GHI reaching the surface; and (vii) integrating the result from item (vi) over all zenith angles for a given day to obtain the daily irradiation, and then integrating over all days in a month or year to obtain the monthly or annual irradiation.

At the altitude of the Tibetan Plateau, the number of air molecules is lower than at sea level, implying that a scaling factor k is required to account for the reduced thickness of the atmosphere. This scaling factor is obtained by taking the ratio of the local pressure and the sea level pressure. The scaling factors $k = 0.64$ and $k = 0.57$ were used for Lhasa and Nagchu, respectively.

As inputs to AccuRT, a scaled and non-scaled US-standard atmosphere were used to simulate radiation at the surface of the high Tibetan Plateau and at sea level surface, respectively. An average Sun-Earth distance was applied, and the atmosphere was divided into 11 and 13 atmospheric layers from a height of 100 km to respectively the surface of the high Tibetan Plateau and the sea level surface. Eight streams were used to solve the RTE in each layer, and the solar zenith angle was set to vary in accordance with time of the year and the geographical location of each site.

2.4. Gaussian smoothing

Gaussian smoothing was applied in order to compare computed high-resolution spectra to the spectra measured with a Ramses sensor (see Section 3.1), which has a spectral resolution of 10 nm.

The Gaussian filter equation is expressed by the following formula:

$$E(\lambda) = \frac{1}{\sigma\sqrt{2\pi}} e^{-\frac{(\lambda-\lambda_0)^2}{2\sigma^2}}, \quad (1)$$

where λ_0 is the average value and σ is the standard deviation. The relationship between the Full Width Half Maximum (FWHM) and the standard deviation is FWHM $\approx 2.36\sigma$.

A standard deviation of 4.25 was applied since the FWHM of Ramses sensor was 10 nm.

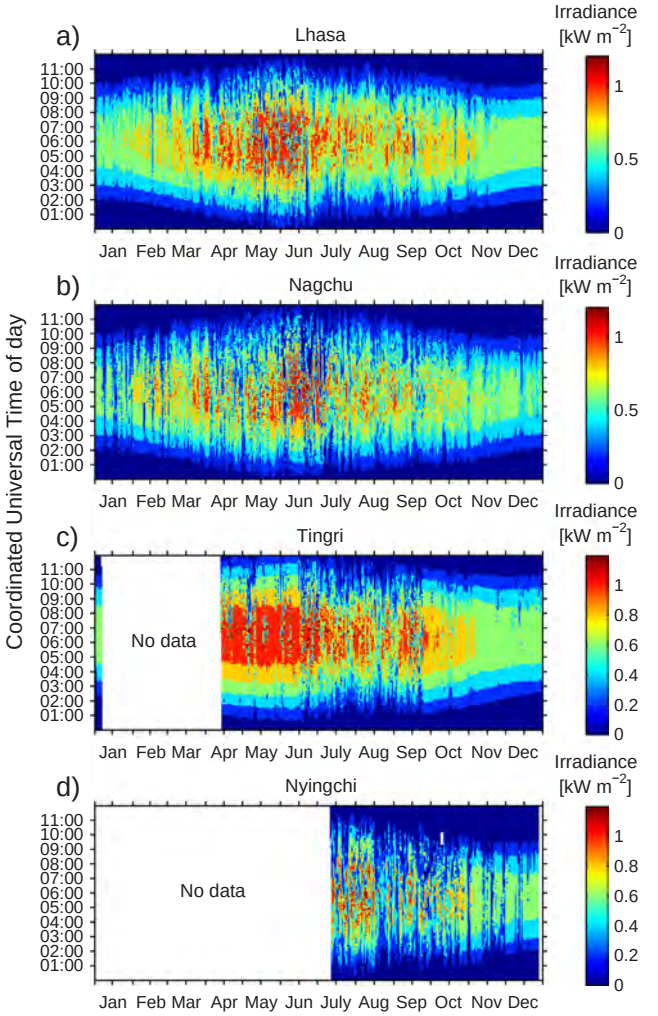

Fig. 3. Daily GHI averaged over all measured years for (a) Lhasa, (b) Nagchu, (c) Tingri, and (d) Nyingchi. Time on the vertical axis is given as UTC, where local noon is around 06:00 UTC.

3. Results and discussion

3.1. GHI measurements

We have analyzed GHI measurements in Lhasa, Nagchu, Tingri, and Nyingchi. Fig. 3 shows GHIs averaged over all measurements at each of the four sites. At around 06:00 universal time coordinated (UTC), corresponding to local noon, the fluctuating patterns show that cloud-free days are more frequent in the wintertime. In Lhasa (Fig. 3a), high GHI values were measured more frequently during April–June than during the rest of the year. In spite of a distinct rainy season from mid June to the end of September, Tingri (Fig. 3c) has many sunshine hours and little influence from clouds for the rest of the year.

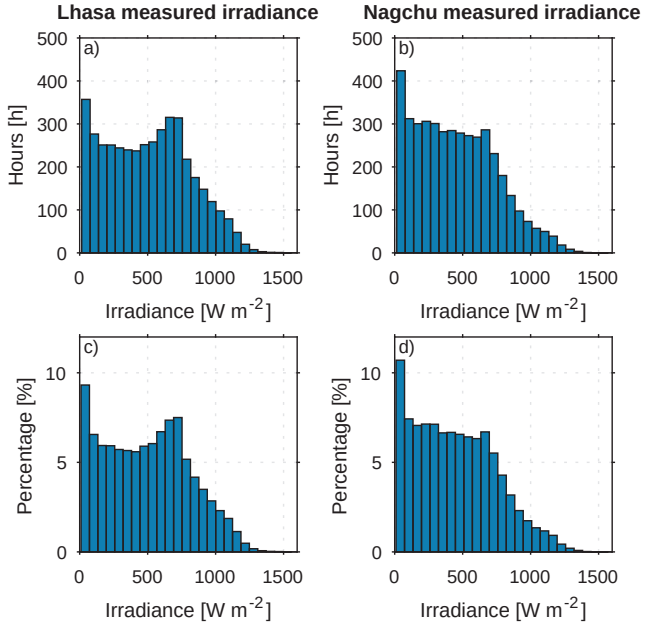

Fig. 4. Measured day time GHI levels and corresponding sunshine hours in one year in Lhasa (a) and Nagchu (b). Measured day time GHI levels and corresponding percentage value in one year in Lhasa (c) and Nagchu (d).

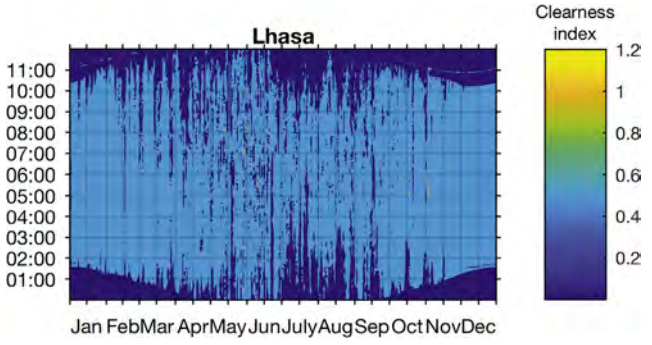

Fig. 5. Daily clearness index averaged over all measured years for Lhasa. Time on the vertical axis is given as UTC.

In Lhasa and Nagchu, about 31 (0.78%) and 33 (0.75%) hours, respectively, in a year have GHI values above 1200 W m^{-2} (Fig. 4).

The maximum values observed in Lhasa and Nagchu are 1558 and 1569 W m^{-2}, respectively, whereas the maximum GHI at TOA is about 1300 W m^{-2} (accounting for the solar zenith angle cosine factor). The annual total duration of measured one-minute GHI values exceeding 1300 W m^{-2} at each of these two sites can reach 6–7 h. The clearness index is defined as the ratio of measured surface GHI and TOA GHI. After calculation, the clearness index values over 1 in Lhasa and Nagchu did not show any concentration in the winter time, this means chronical ground albedo enhancement (e.g. snow on the mountain) can not account for this high GHI values (Fig. 5). This phenomenon can be explained by an enhancement effect caused by broken bright clouds. When such clouds are surrounding the sun, but not blocking it, the diffuse radiation increases as a result of strong scattering (Gueymard, 2017).

Taking all available measurements into account, the yearly averaged daily irradiation values were found to be 5.8 and 5.3 kWh m^{-2} for Lhasa and Nagchu, respectively (averaged from 2010 to 2013). With less than one year of data, averaged daily irradiation values for Tingri and Nyingchi were found to be 6.4 and 4.4 kWh m^{-2}, respectively. In comparison, the five year averaged daily irradiation was found to be about 5.8 kWh m^{-2} in Gaize (32.30 °N, 4700 m, northwestern Tibet)

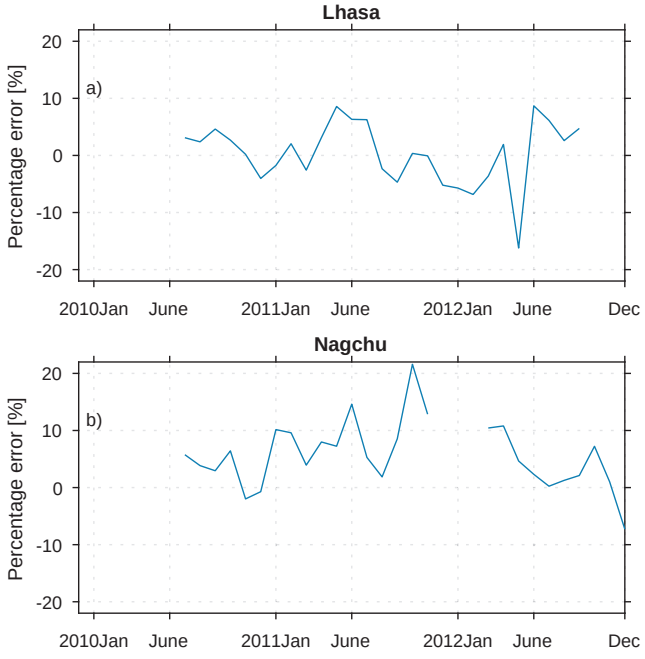

Fig. 6. Percentage error between satellite-derived daily irradiation and measured monthly mean daily irradiation for Lhasa (a) and Nagchu (b).

(Liu et al., 2012), a result that is in good agreement with our measurements. In a solar resource investigation of 89 stations in Chile, one station (Parinacota, 4400 m) had comparable altitude with the Tibetan Plateau. Parinacota was reported to have a high yearly averaged daily irradiance exposure of 5.3 kW m^{-2}. Moreover, Parinacota has a climate with high number of clear days, indicating good solar energy resources with smaller influence by clouds and aerosol (Ortega et al., 2010).

Fig. 6 shows the difference between the monthly mean daily irradiation estimated from Photovoltaic Geographical Information System (PVGIS) and our ground measurement during the same measurement period from 2010 to 2012. The blank period indicates the lack of measured data. The mean absolute percentage difference is 4.3% for Lhasa and 6.4% for Nagchu. Hereby, these satellite-derived estimates were quality assessed by our ground measurements.

In Table 1, the average of all available measurements in 2010, 2011, 2012, and 2013 are shown for Lhasa and Nagchu. In Lhasa, about 7.6 GJ energy can be obtained per square meter horizontal surface in a year, whereas in Nagchu the corresponding amount is about 10% less, i.e. 6.8 GJ. For the observation period from mid April to the end of December, Tingri had the highest irradiation (about 5% higher than Lhasa and 20% higher than Nagchu). The irradiation for the period from mid July to the end of December indicates that Nyingchi has a value that is 21, 13, and 18% lower than the values found for Tingri, Nagchu, and Lhasa, respectively.

3.2. Aerosol influence on solar energy at the ground

At a given site, the yearly averaged aerosol modification factor (YAMF) describes the influence of aerosols on the yearly received solar energy at the ground. The YAMF is defined as the ratio of the modeled annual irradiation obtained for a given aerosol optical depth to the modeled annual irradiation obtained for an atmosphere with no clouds and no aerosols. First, we determined one aerosol optical depth (AOD) as yearly averaged value for each of the four sites (Chengdu, Bejing, Lhasa, and Shegatse) by fitting modeled spectra, generated by AccuRT, to measured spectra. Second, for each of the four sites, we obtained the annual irradiation corresponding to the AOD determined above using AccuRT. Third, for each of the four sites, we obtained the annual

Table 1
Altitude and latitude at seven different sites together with observed and modeled annual irradiation and annual solar energy loss for various atmospheric conditions.

	Lhasa	Nagchu	Tingri	Nyingchi	Shegatse	Chengdu	Beijing
Altitude [m]	3683	4510	4335	2995	3837	500	50
Latitude [°N]	29.65	31.47	28.66	29.66	29.25	30.68	39.93
Observed annual irradiation [GJ m^{-2}]	7.6	6.8	Lack of data	Lack of data	Lack of data	Lack of data	Lack of data
Observation period (14th April to 31st December) [GJ m^{-2}]	5.7	5.0	6.0	Lack of data	Lack of data	Lack of data	Lack of data
Observation period (12th July to 28th December) [GJ m^{-2}]	3.3	3.1	3.4	2.7	Lack of data	Lack of data	Lack of data
Modeled TOA annual irradiation [GJ m^{-2}]	11.3	11.1	11.4	11.3	11.3	11.2	10.1
Modeled annual irradiation without aerosols and clouds [GJ m^{-2}]	8.9	8.8	9.0	8.8	8.9	8.0	7.1
Modeled cloud-free annual irradiation with aerosols [GJ m^{-2}]	8.6	Lack of data	Lack of data	Lack of data	8.6	7.3	4.6
Annual irradiation loss due to atmospheric gases [%]	21	21	21	22	21	29	30
Annual irradiation loss due to aerosols (1-YAMF) [%]	3	Lack of data	Lack of data	Lack of data	3	9	35
Annual irradiation loss due to clouds and aerosols (1-YCAMF) [%]	15	23	Lack of data	Lack of data	Lack of data	Lack of data	Lack of data

irradiation for an atmosphere without aerosols and clouds using AccuRT. Finally, for each of the four sites, we got the YAMF as the annual irradiation obtained for the yearly averaged AOD of the site divided by the annual irradiation obtained for an atmosphere without aerosols and clouds. YAMF can therefore act as an assessment tool to evaluate whether the target location is suitable to plant PV system based on aerosol influence to local receivable solar energy.

3.2.1. Solar spectrum measurements

RAMSES-ACC-VIS and RAMSES-ACC-UV were used to measure the downward spectral GHI every minute during a certain time period in July 2015 (Fig. 7).

The disagreement between the spectra plotted in red and green might be caused by calibration inaccuracy of the instruments and possibly alignment errors of the two radiometers. For Chengdu (Fig. 7a), the measured spectra are probably affected by a varying thin cloud layer. However, for Lhasa (Fig. 7c), the spectra are almost identical, having no cloud influence during the 15-min measurement period around 06:00 UTC (local noon). For Beijing, Fig. 7b shows a corresponding reduction of the spectral GHIs, which are significantly lower than those for the other sites. The reason for this significant spectral reduction may be due to absorption by pollutants in the Beijing atmosphere. On 8th of July 2015, the Beijing was ranked as moderately polluted, according to China's Ministry of Environmental Protection

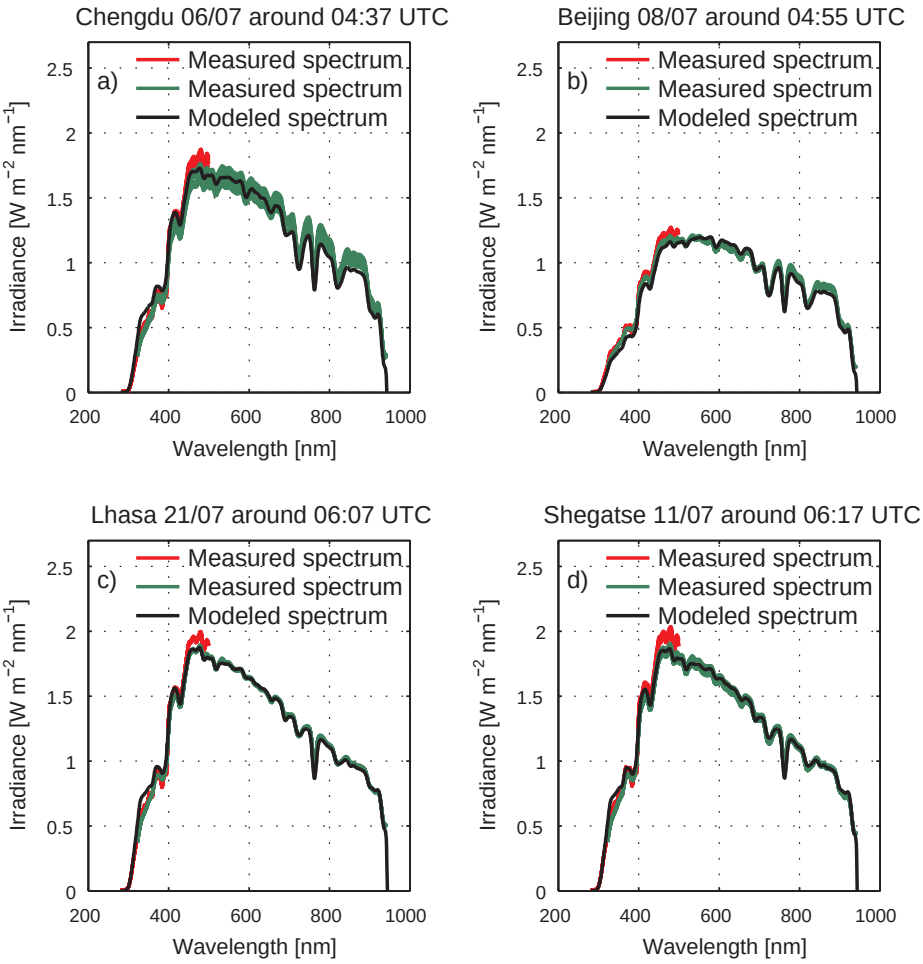

Fig. 7. Measured spectra by RAMSES-ACC-UV (red line) and by RAMSES-ACC-VIS (green line) for 15 min around local noon at Chengdu, Beijing, Lhasa, and Shegatse in July 2015. The solar zenith angle for the four sites are 10.6°, 19.0°, 8.6°, and 7.3° respectively. (For interpretation of the references to colour in this figure legend, the reader is referred to the web version of this article.)

(MEP).We include Beijing here to build a recognition of how strong aerosol attenuates solar irradiance in the capital of China. As mentioned above, China has the largest share of global total installed PV capacity, it is interesting to compare the solar energy reduced by aerosol in different regions. In order to gain knowledge about different aerosol impacts on irradiances in Chengdu, Beijing, Lhasa, and Shegatse, the transmittance at each of these four sites was estimated in Section 3.2.3. The transmittance of the atmosphere at these four sites is obtained as the ratio between an optimized modeled surface spectral GHI fitted to measurements and the TOA spectral GHI.

3.2.2. AOD values at four sites

We used AccuRT to model spectral GHIs in Chengdu, Beijing, Lhasa, and Shegatse and required that the modeled spectral GHIs should agree with the measurements. AccuRT employs Mie calculations to generate aerosol inherent optical properties (IOPs) for given size distributions and refractive indices of aerosol particles. The Mie calculations are based on a code proposed by Du (Du, 2004). A bi-modal lognormal volume size distribution aerosol model was first proposed by Davies (1974), and then further developed by Ahmad et al. (2010). This aerosol model is employed in AccuRT with particle radii for the fine and coarse particle modes chosen to be the two maxima of the bi-modal size distribution. The size distribution is flexible in AccuRT, implying that the centres and heights of the two maxima of the bi-modal size distribution can be freely chosen.

Our fitting process is based on the following guiding principles, supplemented with manual adjustment: (1) The major contribution to scattering is due to fine-mode particles (Larson and Cass, 1989); (2) Mie scattering is the most important particle scattering phenomenon in the atmosphere; and (3) Light attenuation due to scattering is proportional to the wavelength of the incoming light. During the fitting process, the refractive indices for fine and coarse mode aerosols remain fixed (fine mode: $n_r = 1.52; n_i = 0.0097$; coarse mode: $n_r = 1.49; n_i = 0.000001$), whereas the aerosol volume fraction, the fine mode particle radius, and the proportion of fine mode particles (i.e. the fine-mode fraction) are varied. The coarse mode particle radius is fixed ($r_c = 2.492$mm) during fitting. The fitting process extracted out reasonable aerosol size and AOD values in Tibet and Beijing compared to existing measurements. One study shows that the variation of the daily AOD at 500 nm is less than 0.1 at the Namco site (Tibet) during March to May (Cong et al., 2015). The AOD at 588 nm varies from 0.11 to 0.27 over the northern part of the Tibetan Plateau from winter to spring (Xia et al., 2008). In a region that is 162 km away from Lhasa, AOD measurements performed by a multi-spectral photometer gave very low values (less than 0.1) during May and June 1998 (Junhua et al., 2000). From August 2004 to September 2005, an extensive AOD measurement campaign on the Tibetan Plateau showed the smallest mean AOD at 500 nm to be around 0.15. The second cleanest region was found to be the remote northeast corner of China with AOD values ranging from 0.19 to 0.21 (Xin et al., 2007). Because of the rapid change of aerosols, one study measured the aerosol particle size distribution in Beijing all year around. The geometric diameters of the majority of all particles were found to be in the range from 0.01 μm to 0.1 μm. In spring and winter, the majority of all particle diameters at noon were found to be less than 10 nm (Wu et al., 2008). Table 2 indicates that, compared to the other three sites, Beijing had a large amount of extra small fine-mode particles. This fitted result is representative of a heavily polluted hazy air condition in Beijing.

The fitting process resulted in AOD values (at 588 nm) of 0.29, 0.47, 0.09, and 0.13 for Chengdu, Beijing, Lhasa, and Shegatse, respectively. The AOD for Chengdu could also be influenced by thin clouds, although this kind of weather is considered to very good and very rare in Chengdu. For each site, we used AccuRT to obtain the best-fit spectrum, and then we applied Gaussian smoothing using 1 nm sampling and a bandwidth of 4.5 nm, to obtain each of the black curves in Fig. 7.

Table 2
Aerosol characteristics for sites in mainland China and on the Tibetan Plateau.

	Chengdu	Beijing	Lhasa	Shegatse
Particle radius fine mode [μm]	0.13	0.023	0.13	0.13
Particle radius coarse mode [μm]	2.5	2.5	2.5	2.5
Aerosol volume fraction	$3.5{\cdot}10^{-11}$	$8.1{\cdot}10^{-10}$	$1.0{\cdot}10^{-11}$	$1.5{\cdot}10^{-11}$
Fine mode fraction	0.9	0.8	0.99	0.99

3.2.3. Aerosol influence on annual irradiation

We calculated annual irradiation values for a cloud-free sky (eighth row in Table 1) using the AOD values obtained in Section 3.2.2 for Chengdu, Beijing, Lhasa, and Shegatse, respectively. Also, we calculated annual irradiation values for days with no clouds and no aerosols (seventh row in Table 1) in order to determine the YAMF. Table 1 shows a reduction of the annual irradiation by 35% due to highest AOD value of 0.47 in Beijing. In contrast, Chengdu, Lhasa, and Shegatse had much less aerosols for a cloud-free sky. Xia et al. (Xia et al., 2008) found that the AOD over the northern part of the Tibetan Plateau shows distinct seasonal variations. Based on their conclusions, we conducted a sensitivity study by varying the AOD over the Tibetan Plateau to understand the impact of aerosols on the GHI at the ground. The AOD varies significantly in northern Tibet throughout the year due to impact from the Taklimakan Desert (Xia et al., 2008). In southern Tibet, the influence from the Taklimakan Desert is believed to be less, and the AOD is mainly caused by the burning of juniper wood and leaves for religious purposes.

The AOD at 588 nm varies from 0.11 to 0.27 over the northern part of Tibetan Plateau from winter to spring (Xia et al., 2008). As shown in Fig. 8, this AOD variation reduces the corresponding annual irradiation by between 3% and 6% at all four sites in Tibet under cloud-free sky. These results apply specifically for four sites with corresponding gases composition including water vapor in the air of each four sites.

To gain information about the influence of the atmospheric composition in Chengdu, Bejing, Lhasa, and Shegatse, we modeled the solar spectral GHI at the TOA to assess the spectral transmittance. The transmittance is the ratio of the modeled spectral GHI at the Earth's surface to the modeled spectral GHI at the TOA. The spectral transmittance of the atmosphere is displayed in Fig. 9 for Chengdu, Beijing, Lhasa, and Shegatse. The solar zenith angles of the measurements deviate from the highest solar zenith angle less than 2.6°. The solar zenith angles for the four sites are 10.6°, 19.0°, 8.6°, and 7.3°for Chengdu, Beijing, Lhasa, and Shegatse, respectively, whereas on July 6th, the highest solar zenith angles are 8.0°, 17.2°, 6.9°, and 6.5°, respectively. For Beijing, due to its relatively high latitude (39 °N), the sun reaches its highest elevation of 17.2°during July. In addition to aerosols, the most important atmospheric gases that reduce sunlight in the spectral region from 300 to 950 nm are O_3, O_2, and H_2O. Fig. 9 shows the specific wavelength regions in which sunlight is absorbed by O_3, O_2, and H_2O

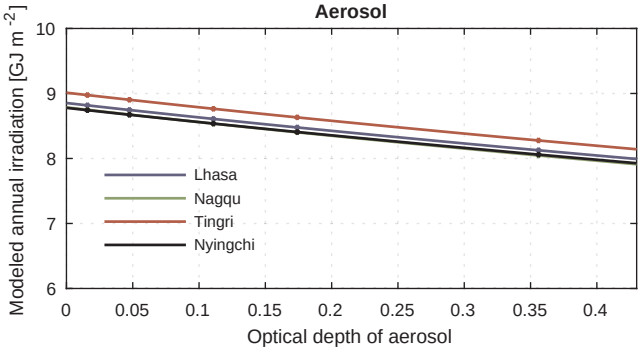

Fig. 8. Sensitivity of the annual irradiation to the aerosol optical depth in Lhasa, Nagchu, Tingri, and Nyingchi.

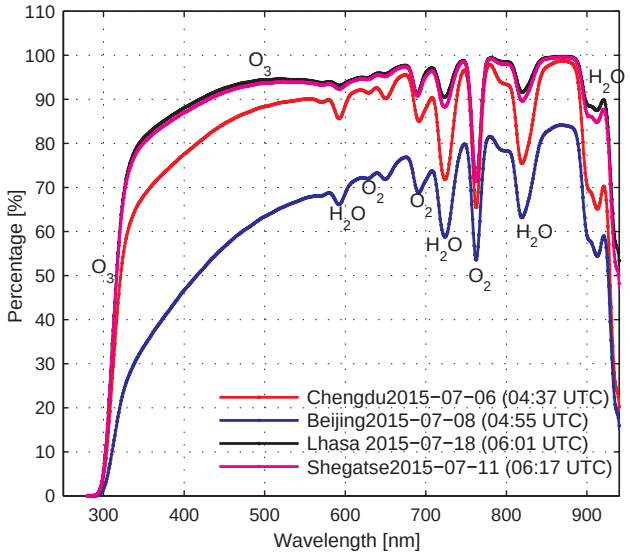

Fig. 9. Modeled atmospheric transmittance in Chengdu, Beijing, Lhasa, and Shegatse at solar zenith angle of 10.6°, 19.0°, 8.6°, and 7.3°, respectively. The absorption bands of different gases are marked in the figure.

molecules. Rayleigh scattering is responsible for the attenuation in the short wavelength range. Also, Fig. 9 shows that on the days the measurements were made, Lhasa and Shegatse had the most transparent atmosphere, and Lhasa had the smallest water vapour absorption. Due to the high AOD, the transmittance for Beijing was considerably lower than at the other sites. Also, the absorption by water vapour was considerably higher in Beijing and Chengdu than in Lhasa and Shegatse.

3.3. Yearly averaged cloud/aerosol modification factor (YCAMF)

In order to gain information about aerosol and cloud combined effect to solar energy in Lhasa and Nagchu, we used AccuRT to estimate the yearly averaged cloud/aerosol modification factor (YCAMF) for these two sites. The YCAMF is the ratio of the observed annual irradiation to the modeled yearly irradiation that would be obtained for an atmosphere with no clouds and no aerosols throughout a whole year.

3.3.1. Yearly modeled GHI

If an atmosphere with no clouds or aerosols prevailed throughout a whole year, the annual irradiation values in Lhasa, Nagchu, Tingri, and Nyingchi would be as shown in Table 1 (seventh row), which also shows observed annual irradiation values at these sites (third fourth and fifth rows).

From Table 1, the annual irradiation is reduced by 15% and 23% by aerosols and clouds in Lhasa and Nagchu, respectively. Thus, Nagchu is influenced by clouds and aerosols more frequently than Lhasa. Based on the available data, the solar energy in Tingri was found to be reduced by just 12% due to clouds and aerosols.

4. Conclusions

Four sites in Tibet were chosen for measurements of GHI. The measurements indicate a large solar energy potential on the Tibetan Plateau, with GHI values approaching 1300 W m^{-2} at summer noon under cloud-free sky condition, which are comparable with the values at TOA (1368 W m^{-2}). A small portion of GHI values even exceeded the TOA GHI in situations with blue sky and with neighboring clouds that did not obstruct the line of sight. Tingri had the largest solar energy potential among the four study sites, and Nyingchi had the lowest. Lhasa had a larger solar energy potential than Nagchu.

Within the time frame of a year, Lhasa was found to have a higher annual irradiation (7.6 GJ m^{-2}) than Nagchu (6.8 GJ m^{-2}). Spectral transmittances were estimated by use of a radiative transfer model (AccuRT). The atmosphere above the two sites in Tibet was much more transparent than above the two sites investigated in mainland China (Beijing and Chengdu), making the solar energy potential on the Tibetan Plateau promising for use of solar energy devices.

The solar energy potential on the Tibetan Plateau is affected by cloud and aerosol, AccuRT was used to quantify the influence of each of these factors. The cloud and aerosol free sky annual irradiation was estimated to be reduced by aerosols by 3–6% for a typical range of AOD values in Tibet (0.17–0.27 at 588 nm). Clouds and aerosols were found to reduce the annual irradiation by 15% (1.3 GJ m^{-2}) in Lhasa and 23% (2.0 GJ m^{-2}) in Nagchu.

In this paper, four sites in Tibet were chosen for GHI data collection. As future work, it would be useful to conduct measurements in Tingri for at least one complete year, and also try to find other sites that may have an even larger solar energy potential than Tingri. Also, it would be interesting to study the effect that the orientation of a solar panel may have on the amount of captured solar energy, and, hence, on the electricity production. This type of investigation can be initiated by modeling the angular distribution of the diffuse downward radiance. In particular, it would be useful for a site having a high surface albedo to capture more light by solar panels. In this study, spectral GHI measurements (in contrast to broad-band GHI) were only conducted during one day in Tibet and mainland China. But in general, the atmospheric properties, such as the aerosol size distribution and the amount of water vapour, vary with time. Thus, future investigations of long term atmospheric properties in Tibet would be useful and important for assessment of the solar energy potential on the Tibetan Plateau.

Acknowledgments

This research is supported by the National Natural Science Foundation of China (project code: 41475139), the Network for University Cooperation Tibet-Norway (Environmental Physics in Tibet, Project code: 120112), the Mt. Everest Scholar's Training Program of Tibet University (project name: Norsang Gelsor and Tsoja Wangmo) and the Environment Control and Green Energy Saving Design of Plateau Human Settlements project of Tibet University.

References

AccuRT, 2017. Accurt – accurate radiative transfer software. http://www.geminor.com (accessed 16.12.30).

Ahmad, Z., Franz, B.A., McClain, C.R., Kwiatkowska, E.J., Werdell, J., Shettle, E.P., Holben, B.N., 2010. New aerosol models for the retrieval of aerosol optical thickness and normalized water-leaving radiances from the SeaWiFS and MODIS sensors over coastal regions and open oceans. Appl. Opt. 49, 5545–5560.

BOM, 2017. Bureau of meteorology of australian government. https://www.nrel.gov/docs/fy12osti/54824.pdf (Last updated 16 November 2017).

Calinoiu, D., Paulescu, M., Ionel, I., Stefu, N., Pop, N., Boata, R., Pacurar, A., Gravila, P., Paulescu, E., Trif-Tordai, G., 2013. Influence of aerosols pollution on the amount of collectable solar energy. Energy Convers. Manage. 70, 76–82.

Cebecauer, T., Suri, M., 2016. Site-adaptation of satellite-based DNI and GHI time series: overview and SolarGIS approach. In: AIP Conference Proceedings. AIP Publishing, pp. 150002.

Chen, J.L., Xiao, B.B., Chen, C.D., Wen, Z.F., Jiang, Y., Lv, M.Q., Wu, S.J., Li, G.S., 2014. Estimation of monthly-mean global solar radiation using modis atmospheric product over china. J. Atmos. Solar Terr. Phys. 110, 63–80.

CMA, 2017. China meteorological administration. http://www.cma.gov.cn (accessed 17.11.30).

Cong, Z., Kang, S., Kawamura, K., Liu, B., Wan, X., Wang, Z., Gao, S., Fu, P., 2015. Carbonaceous aerosols on the south edge of the tibetan plateau: concentrations, seasonality and sources. Atmos. Chem. Phys. 15, 1573–1584.

Davies, C., 1974. Size distribution of atmospheric particles. J. Aerosol Sci. 5, 293–300.

Du, H., 2004. Mie-scattering calculation. Appl. Opt. 43, 1951–1956.

Europe, S.P., 2016. Global market outlook for solar power 2016–2020. Solar Power Europe: Bruxelles, Belgium, 32.

Gueymard, C.A., 2017. Cloud and albedo enhancement impacts on solar irradiance using high-frequency measurements from thermopile and photodiode radiometers. Part 2: Performance of separation and transposition models for global tilted irradiance. Sol. Energy.

Hamre, B., Stamnes, S., Stamnes, J.J., Stamnes, K., 2014. AccuRT: A Versatile Tool for

Radiative Transfer in Coupled Media like Atmosphere-Ocean Systems. In: Ocean Optics XXII, Portland, ME, USA.
He, G., Kammen, D.M., 2016. Where, when and how much solar is available? A provincial-scale solar resource assessment for china. Renew. Energy 85, 74–82.
Jaques, L., Bradshaw, M., Carson, L., Budd, A., Huleatt, M., Hutchinson, D., Lambert, I., LePoidevin, S., McKay, A., Miezitis, Y., Sait, R., Zhu, R., Hughes, M., 2010. Solar Energy. Aust. Energy Resour. Assess. 261–284.
Junhua, Z., Li, L., Jietai, M., 2000. Remote sensing of aerosol optical properties with multi-spectral sun photometer in the Damxung region, tibetan plateau [j]. SCIENTIA ATMOSPHERICA SINICA 4, 010.
Larson, S.M., Cass, G.R., 1989. Characteristics of summer midday low-visibility events in the Los Angeles area. Environ. Sci. Technol. 23, 281–289.
Li, H., Ma, W., Lian, Y., Wang, X., Zhao, L., 2011. Global solar radiation estimation with sunshine duration in Tibet, China. Renew. Energy 36, 3141–3145. https://doi.org/10.1016/j.renene.2011.03.019.
Liu, J.D., Liu, J.M., Linderholm, H.W., Chen, D.L., Yu, Q., Wu, D.R., Haginoya, S., 2012. Observation and calculation of the solar radiation on the Tibetan Plateau. Energy Convers. Manage. 57, 23–32. https://doi.org/10.1016/j.enconman.2011.12.007.
Long, C.N., Shi, Y., 2008. An automated quality assessment and control algorithm for surface radiation measurements. Open Atmos. Sci. J. 2.
Mayer, B., Kylling, A., 2005. The libradtran software package for radiative transfer calculations-description and examples of use. Atmos. Chem. Phys. 5, 1855–1877.
Neckel, H., et al., 1981. Improved data of solar spectral irradiance from 0.33 to 1.25 μ. In: Phys. Solar Var. Springer, pp. 231–249.
Ortega, A., Escobar, R., Colle, S., De Abreu, S.L., 2010. The state of solar energy resource assessment in chile. Renew. Energy 35, 2514–2524.
Polo, J., Wilbert, S., Ruiz-Arias, J.A., Meyer, R., Gueymard, C., Suri, M., Martín, L., Mieslinger, T., Blanc, P., Grant, I., et al., 2016. Preliminary survey on site-adaptation techniques for satellite-derived and reanalysis solar radiation datasets. Sol. Energy 132, 25–37.
Sengupta, M., Habte, A., Gueymard, C., Wilbert, S., Renne, D., 2017. Best practices handbook for the collection and use of solar resource data for solar energy applications. Technical Report. National Renewable Energy Lab.(NREL), Golden, CO (United States).
Stamnes, K., Thomas, G.E., Stamnes, J.J., 2017. Radiative Transfer in the Atmosphere and Ocean. 2 ed. Cambridge University Presshttps://doi.org/10.1017/9781316148549.
Suri, M., Cebecauer, T., 2014. Satellite-based solar resource data: Model validation statistics versus user's uncertainty. In: ASES SOLAR 2014 Conference, San Francisco, pp. 7–9.
Tang, W., Yang, K., He, J., Qin, J., 2010. Quality control and estimation of global solar radiation in China. Sol. Energy 84, 466–475. https://doi.org/10.1016/j.solener.2010.01.006.
Thornton, P.E., Running, S.W., 1999. An improved algorithm for estimating incident daily solar radiation from measurements of temperature, humidity, and precipitation. Agric. For. Meteorol. 93, 211–228. https://doi.org/10.1016/S0168-1923(98)00126-9.
Tutiempo, 2016. Averaged precipitation value from 2001 to 2013. http://www.tutiempo.net/ (accessed 16.7.30).
Wang, Q., Qiu, H.N., 2009. Situation and outlook of solar energy utilization in Tibet, China. Renew. Sustain. Energy Rev. 13, 2181–2186. https://doi.org/10.1016/j.rser.2009.03.011.
WeatherChina, 2016. Weather china official website. http://www.weather.com.cn (accessed: 16.10.30).
Wehrli, C., 1985. Physikalisch-meteorologisches observatorium and world radiation center, davos, switzerland.
Wilcox, S., 2012. National solar radiation database 1991–2010 update: User's manual. https://www.nrel.gov/docs/fy12osti/54824.pdf.
WRDC, 2016. World radiation data centre. http://wrdc.mgo.rssi.ru/wwwrootnew/publ/WRDC_issue_2016_2.pdf (accessed 17.11.30).
Wu, Z., Hu, M., Lin, P., Liu, S., Wehner, B., Wiedensohler, A., 2008. Particle number size distribution in the urban atmosphere of Beijing, China. Atmos. Environ. 42, 7967–7980.
Xia, X., Wang, P., Wang, Y., Li, Z., Xin, J., Liu, J., Chen, H., 2008. Aerosol optical depth over the Tibetan Plateau and its relation to aerosols over the Taklimakan Desert. Geophys. Res. Lett. 35, 1–5. https://doi.org/10.1029/2008GL034981.
Xin, J., Wang, Y., Li, Z., Wang, P., Hao, W.M., Nordgren, B.L., Wang, S., Liu, G., Wang, L., Wen, T., et al., 2007. Aerosol optical depth (AOD) and ångström exponent of aerosols observed by the Chinese Sun Hazemeter Network from August 2004 to September 2005. J. Geophys. Res.: Atmos. 112.
Yang, K., Koike, T., Ye, B., 2006. Improving estimation of hourly, daily, and monthly solar radiation by importing global data sets. Agric. For. Meteorol.